

Constraining the nuclear symmetry energy from electric dipole polarizability and neutron skin in ^{208}Pb within antisymmetrized molecular dynamics

Dandan Niu,¹ Xinyu Wang,¹ Ying Cui,¹ Qiang Zhao,¹ Kai Zhao,¹ Akira Ono,² and Yingxun Zhang^{1,3,4,*}

¹*China Institute of Atomic Energy, Beijing 102413, China*

²*Department of Physics, Graduate School of Science, Tohoku University, Sendai 980-8578, Japan*

³*Guangxi Key Laboratory of Nuclear Physics and Technology,
Guangxi Normal University, Guilin, 541004, China*

⁴*Southern Center for Nuclear-Science Theory (SCNT),
Institute of Modern Physics, Chinese Academy of Sciences, Huizhou 516000, China*

(Dated: February 24, 2026)

The electric dipole polarizability α_D and the neutron skin thickness ΔR_{np} of ^{208}Pb are two powerful and clean probes to constrain the symmetry energy at subsaturation density. Within the framework of the antisymmetrized molecular dynamics (AMD) model, we found that the sensitive densities of α_D and ΔR_{np} ranges from the $0.2\rho_0$ to $0.57\rho_0$. To well describe the data of α_D and ΔR_{np} , the effective interaction parameters with $S_0 \sim 34$ MeV and $L = 66 - 75$ MeV are favored. The constraints of symmetry energy over the density ranging from $0.2\rho_0$ to $0.57\rho_0$ are obtained, and the values of symmetry energy at the starting and ending density region are $S(\rho = 0.2\rho_0) = 10.5 \pm 0.63$ MeV and $S(\rho = 0.57\rho_0) = 23.1 \pm 0.4$ MeV.

I. INTRODUCTION

The nuclear symmetry energy characterizes the isospin dependence of the isospin asymmetric nuclear equation of state, which is described by the energy per nucleon of the isospin asymmetric nuclear matter. Theoretically, it can be approximately written as

$$E/A(\rho, \delta) \approx E/A(\rho, \delta = 0) + S(\rho)\delta^2. \quad (1)$$

The first term in the right hand side is the equation of state for symmetric nuclear matter, and the second term is the symmetry energy, which plays a crucial role in our understanding of the properties of neutron stars, the heavy ion collision mechanism and observables, and the ground and collective excited state properties of nuclei. However, theoretical predictions on the density dependence of symmetry energy $S(\rho)$ have large uncertainties away from the normal density, and thus constraining the density dependence of symmetry energy $S(\rho)$ has become one of the main goals in nuclear physics [1, 2].

Considerable efforts have been devoted to constraining the nuclear equation of state and nuclear symmetry energy, and comprehensive reviews on this subject can be found in Refs. [3, 4]. In nuclear astrophysics, the most commonly employed observables include the mass-radius relation of neutron stars and their tidal deformabilities [4–9]. In the context of heavy-ion collisions [10–13], a variety of isospin-sensitive observables have been proposed to probe the symmetry energy, such as neutron to proton yield ratios [14, 15], isospin diffusion [9–11, 16, 17], and charged pion yield ratios [18–20]. In nuclear structure studies, observables including the neutron skin thickness ΔR_{np} [21–25], the isovector giant dipole

resonance (IVGDR) and the electric dipole polarizability α_D [26–33], the pygmy dipole resonance (PDR) [34–37], and the isoscalar and isovector giant quadrupole resonances (ISGQR and IVGQR) [38] have been extensively used to extract constraints on the symmetry energy, particularly at subsaturation densities.

Among these observables, the electric dipole polarizability α_D and the neutron skin thickness ΔR_{np} are widely regarded as two particularly clean and powerful probes of the symmetry energy at subsaturation densities [3, 28, 39]. A consistent description of both observables within a unified theoretical framework is therefore highly desirable. To date, two main classes of models have been employed toward this goal. One is the random-phase approximation (RPA) based on relativistic or non-relativistic energy density functionals [30, 40, 41]. Using such approaches, constraints on the symmetry energy around saturation and subsaturation densities have been extracted, for example $S(\rho_0) = 30 - 35$ MeV [41] and $S(\rho_0/3) = 15.91 \pm 0.99$ MeV [30]. However, only a limited number of models are able to simultaneously reproduce both the IVGDR data and the PREX-II neutron skin result for ^{208}Pb , with notable exceptions given in Refs. [33, 42].

Another method is to use the transport models, such as extended quantum molecular dynamics (EQMD) [43, 44], Boltzmann-Uehling-Uhlenbeck (BUU) [32, 45–47], isospin-dependent quantum molecular dynamics model (IQMD) [48]. These approaches have been used to constrain symmetry energy, and it is valuable for clarifying the potential reasons for the above mentioned tension and advancing toward a definitive conclusion about its behavior in isospin asymmetric nuclear matter. For example, the analysis based on BUU approach has suggested that the constraints on symmetry energies are $S(\rho_0/3) = 16.4 \pm 1.0$ MeV [49]. In Refs. [32, 45–47], they also provide the favored constraints on the effective mass splitting [32, 45] and in-medium nucleon-nucleon cross

* zhyx@ciae.ac.cn

sections. However, it is hard to describe the neutron skin of ^{208}Pb in QMD-like and BUU-like models, since these models belong to a semi-classical transport models and lack strong Pauli blocking for describing the fermion properties of nucleons as mentioned in Ref. [50]. The antisymmetrized molecular dynamics (AMD) model [51] describes the total wave function as a Slater determinant of Gaussian wave packets with fixed width, thereby preserving the fermionic character of the system and the Pauli principle. The use of such compact wave packets is advantageous for the description of fragment formation in reactions and cluster correlations in nuclei, while the full antisymmetrization provides a sound basis for the description of nuclear ground states and collective excitations. The AMD framework thus offers a unique opportunity to investigate the IVGDR and neutron skin on the same microscopic footing within a transport model description.

In this work, we employ the antisymmetrized molecular dynamics (AMD) model [51, 52] to investigate the isovector giant dipole resonance and neutron skin of ^{208}Pb . The paper is organized as follows. In Sec. II, we briefly describe the theoretical framework of AMD, the effective interaction parameters employed and the method for calculating IVGDR. The main results and discussions are presented in Sec. III, which includes the ground state properties, the calculated strength functions, and the analysis of the correlations between the dipole observables and the symmetry energy. In Sec. IV we give a summary and outlook.

II. THEORETICAL FRAMEWORK

A. AMD Model

The AMD code we used is as the same as in Ref. [53]. For the convenience, we briefly introduce the framework of AMD model and how we incorporate the perturbations and calculate the IVGDR.

In the AMD model, the wave function of an A -nucleon system is given by a Slater determinant,

$$|\Phi\rangle = \frac{1}{\sqrt{A!}} \det[\varphi_i(j)] \quad (2)$$

with

$$\varphi_i = \phi_{\mathbf{Z}_i} \chi_{\alpha_i}, \quad (3)$$

where α_i represents the spin and isospin of the i -th single-particle state, $\alpha_i = p \uparrow, p \downarrow, n \uparrow, \text{ or } n \downarrow$, and χ is the spin and isospin wave function. The spatial part of the i -th single-particle wave function $\phi_{\mathbf{Z}_i}$ is given by a localized Gaussian wave function, whose center is represented by the complex parameter \mathbf{Z}_i ,

$$\phi_{\mathbf{Z}_i}(\mathbf{r}_j) = \left(\frac{2\nu}{\pi}\right)^{3/4} \exp\left[-\nu\left(\mathbf{r}_j - \frac{\mathbf{Z}_i}{\sqrt{\nu}}\right)^2\right], \quad (4)$$

where ν is a parameter to represent the width of the wave packet. For each single-particle wave function, without considering the antisymmetrization effect, it is easily seen that the real part and the imaginary part of \mathbf{Z}_i correspond to the centroids of the position and the momentum,

$$\mathbf{Z}_i = \sqrt{\nu} \frac{\langle \varphi_i | \mathbf{r} | \varphi_i \rangle}{\langle \varphi_i | \varphi_i \rangle} + \frac{i}{2\sqrt{\nu}\hbar} \frac{\langle \varphi_i | \mathbf{p} | \varphi_i \rangle}{\langle \varphi_i | \varphi_i \rangle}. \quad (5)$$

The time evolution of the system is determined by the time-dependent variational principle,

$$\delta \int_{t_1}^{t_2} dt \frac{\langle \Phi(\mathbf{Z}) | i\hbar \frac{d}{dt} - H | \Phi(\mathbf{Z}) \rangle}{\langle \Phi(\mathbf{Z}) | \Phi(\mathbf{Z}) \rangle} = 0. \quad (6)$$

This leads to the equations of motion with respect to \mathbf{Z} ,

$$i\hbar \sum_{j\tau} C_{i\sigma,j\tau} \dot{Z}_{j\tau} = \frac{\partial \mathcal{H}}{\partial Z_{i\sigma}^*} \quad \text{and c.c.}, \quad (7)$$

where $\sigma, \tau = x, y, z$ and \mathcal{H} is the expectation value of the Hamiltonian H with the spurious kinetic energy arising from the zero-point center-of-mass motion of the fragments subtracted [51, 52],

$$\mathcal{H}(\mathbf{Z}, \mathbf{Z}^*) = \frac{\langle \Phi(\mathbf{Z}) | H | \Phi(\mathbf{Z}) \rangle}{\langle \Phi(\mathbf{Z}) | \Phi(\mathbf{Z}) \rangle} - \frac{3\hbar^2\nu}{2M} A + T_0[A - N_F(\mathbf{Z})]. \quad (8)$$

Here $N_F(\mathbf{Z})$ is the fragment number. In our calculations, $\nu = 0.16 \text{ fm}^{-2}$ and $T_0 = 8.2 \text{ MeV}$ for SLy4 and 8.5 MeV for SkM*. The matrix $C_{i\sigma,j\tau}$ is

$$C_{i\sigma,j\tau} = \frac{\partial^2}{\partial Z_{i\sigma}^* \partial Z_{j\tau}^*} \ln \langle \Phi(\mathbf{Z}) | \Phi(\mathbf{Z}) \rangle, \quad (9)$$

which is hermitian and positive definite. The nucleon-nucleon collisions are switched off in this work.

In the present calculations, we adopt the Skyrme-type effective interaction with the spin-orbit term omitted:

$$\begin{aligned} v_{ij} = & t_0(1 + x_0 P_\sigma) \delta(\mathbf{r}) \\ & + \frac{1}{2} t_1(1 + x_1 P_\sigma) [\delta(\mathbf{r}) \mathbf{k}^2 + \mathbf{k}^2 \delta(\mathbf{r})] \\ & + t_2(1 + x_2 P_\sigma) \mathbf{k} \cdot \delta(\mathbf{r}) \mathbf{k} \\ & + \frac{1}{6} t_3(1 + x_3 P_\sigma) [\rho(\mathbf{r}_i)]^\gamma \delta(\mathbf{r}), \end{aligned} \quad (10)$$

where $\mathbf{r} = \mathbf{r}_i - \mathbf{r}_j$ and $\mathbf{k} = \frac{1}{2\hbar}(\mathbf{p}_i - \mathbf{p}_j)$.

To systematically investigate the influence of the symmetry energy coefficient $S_0 = S(\rho_0)$ and the slope of symmetry energy $L = 3\rho_0 \left(\frac{\partial S}{\partial \rho}\right)_{\rho=\rho_0}$ on the IVGDR and ΔR_{np} , we need to construct a kind of effective interactions that can vary S_0 and L with fixed incompressibility K_0 , the isoscalar effective mass m_s^* , and the isovector effective mass m_v^* . Thus, we extend the standard Skyrme interaction by introducing an additional density-dependent interaction terms [54], i.e.,

$$v_{ij}^{\text{ext}} = \frac{1}{6} t_3 x_3 P_\sigma \delta(\mathbf{r}) (\rho(\mathbf{r}_i)^\gamma - \rho_0^\gamma). \quad (11)$$

With this additional term, the symmetry energy takes the form

$$\begin{aligned}
S(\rho) = & \frac{1}{3} \frac{\hbar^2}{2m} \left(\frac{3\pi^2}{2} \right)^{2/3} \rho^{2/3} - \frac{1}{8} t_0 (2x_0 + 1) \rho \\
& - \frac{1}{24} \left(\frac{3\pi^2}{2} \right)^{2/3} (3\Theta_v - 2\Theta_s) \rho^{5/3} \\
& - \frac{1}{48} t_3 (2x_3 \rho_0^\gamma \rho + \rho^{\gamma+1}) \\
& - \frac{1}{24} t_3 x_3' (\rho^{\gamma+1} - \rho_0^\gamma \rho),
\end{aligned} \tag{12}$$

where $\Theta_s = 3t_1 + t_2(5 + 4x_2)$ and $\Theta_v = t_1(2 + x_1) + t_2(2 + x_2)$. By varying x_3 and x_3' , the S_0 and L will change, but the values of the K_0 , m_s^* , and m_v^* are remained.

In the present work, two groups of the effective interactions are adopted, as summarized in Table I. One group corresponds to $m_n^* < m_p^*$ and $f_I = m/m_s^* - m/m_v^* = 0.19$, whereas the other corresponds to $m_n^* > m_p^*$ and $f_I = m/m_s^* - m/m_v^* = -0.26$. This construction allows us to explore not only the effects of S_0 and L , but also the influence of the neutron-proton effective mass splitting. The corresponding values of x_3 and x_3' are listed in Appendix A.

TABLE I. Parameter sets used in the calculations, S_0 and L are in MeV.

Sets	m_s^*/m	m_v^*/m	f_I	S_0	L
1-15	0.695	0.800	0.19	[30, 32, 34]	[46, 61, 75, 92, 108]
16-30	0.789	0.653	-0.26	[30, 32, 34]	[46, 61, 75, 92, 108]

B. Isovector Giant Dipole Resonance

To calculate the IVGDR under the response to external fields, the following procedure is employed: preparing the ground state of the nucleus, applying an external dipole perturbation at the initial moment to the ground state nucleus, following the subsequent time evolution of the system, and then extracting the dipole strength function.

First, we seek the ground state wave function $\Phi_0(\{\mathbf{Z}_i\})$ of the nucleus which is realized by using the frictional cooling method [51, 52]. The cooling step is stopped to identify the ground state when the evaluated energy of the system becomes lower than the experimental energy in case the calculation with the adopted interaction overestimates the binding energy, or an energy minimum is reached.

Then, the collective excitation is induced by boosting the ground state wave function $\Phi_0(\{\mathbf{Z}_i\})$ instantaneously at $t = 0$ with an external perturbative field $V_{\text{ext}}(\mathbf{r}, t) = \epsilon \mathcal{M} \delta(t)$ to give the initial state $\Psi(t = 0^+)$ for time-dependent calculations. The parameter ϵ is the perturbation strength. The external electric dipole field operator is defined using the spherical harmonic $Y_{1\mu}$

($\mu = \pm 1, 0$),

$$\mathcal{M}(E1, \mu) = \sum_{i=1}^A e_i^{\text{rec}} r_i Y_{1\mu}(\hat{\mathbf{r}}_i), \tag{13}$$

where e_i^{rec} is the recoil charge (Ne/A for protons and $-Ze/A$ for neutrons). This method gives the initial state $\Psi(t = 0^+)$ as

$$\Psi(t = 0^+) = \exp[-i\epsilon \mathcal{M}(E1, \mu)/\hbar] \Phi_0, \tag{14}$$

which is the same as in Ref. [55]. It corresponds to a simply transforming the parameters $\mathbf{Z} = \{\mathbf{Z}_1, \mathbf{Z}_2, \dots, \mathbf{Z}_A\}$ as follows:

$$\mathbf{Z}_i(t = 0^+) = \mathbf{Z}_i(t = 0) - i \frac{\epsilon e^{\text{rec}} \sqrt{\frac{3}{4\pi}} \mathbf{e}_\mu}{2\hbar\sqrt{\nu}}, \tag{15}$$

where \mathbf{e}_μ donates the unit vector corresponding to the polarization direction.

Thirdly, the time evolution of $|\Psi(t)\rangle$ is solved by Eq. (7) and the time-dependent dipole moment is obtained as

$$\begin{aligned}
D_\mu(t) & \equiv \frac{\langle \Psi(t) | \mathcal{M}(E1, \mu) | \Psi(t) \rangle}{\langle \Psi(t) | \Psi(t) \rangle} \\
& = \sqrt{\frac{3}{4\pi}} \sum_{i,j=1}^A e_i^{\text{rec}} \mathbf{e}_\mu \cdot \frac{\mathbf{Z}_i^*(t) + \mathbf{Z}_j(t)}{2\sqrt{\nu}} B_{ij} B_{ji}^{-1}
\end{aligned} \tag{16}$$

The $\mathbf{Z}_i(t)$ is the complex variational parameters at time t , and B_{ij} is the overlap matrix of single-particle states in the AMD model. The $D_\mu(t)$ represents the oscillation of the proton-neutron relative motion induced by E1 boost in $\mu = 0, \pm 1$, which corresponds to the collective dipole mode of the system.

Finally, the transition strength distribution is then obtained by the following relationship,

$$\begin{aligned}
S(\omega; E1, \mu) & = -\frac{1}{\pi\epsilon} \text{Im} \int_0^\infty dt \langle \Psi(t) | \mathcal{M}(E1, \mu) | \Psi(t) \rangle e^{i\omega t} \\
& = -\frac{1}{\pi\epsilon} \text{Im} \int_0^\infty dt D_\mu(t) e^{i\omega t}.
\end{aligned} \tag{17}$$

In the practical calculation, we impose the $E1$ field with respect to z direction ($\mu = 0$). This perturbation corresponds to a small momentum boost induced by the dipole field. The corresponding dipole moment is written as,

$$D_{\mu=0}(t) = \sqrt{\frac{3}{4\pi}} e \frac{NZ}{A} (R_{p,\mu=0}(t) - R_{n,\mu=0}(t)), \tag{18}$$

where $R_{p,\mu=0}(t)$ and $R_{n,\mu=0}(t)$ are the $\mu = 0$ components of the centers of mass of protons and neutrons, respectively. Then, the corresponding transition strength function, $S(\omega; E1, \mu = 0)$, can be obtained with Eq. (17). The total strength function will be obtained with

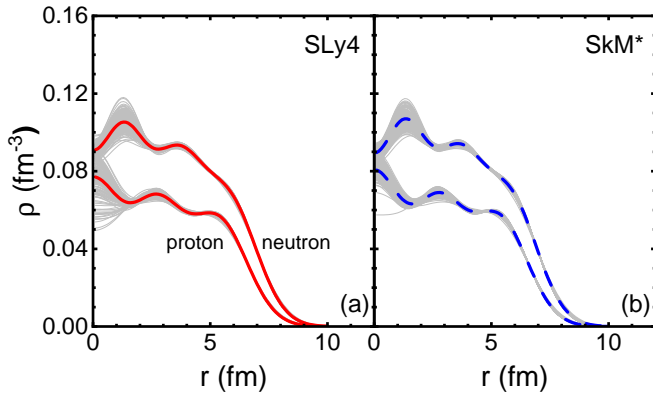


FIG. 1. Radial density distributions of neutrons and protons for ^{208}Pb . Thin lines are the results obtained by AMD from 200 events, and thick lines are the event averaged values. Left panel is for SLy4, and right panel is for SkM*.

$$S(\omega; E1) = 3S(\omega; E1, \mu = 0). \quad (19)$$

Once the strength function of IVGDR is obtained, the electric dipole polarizability α_D is calculated as

$$\alpha_D = \frac{8\pi}{9} \int \frac{S(\omega)}{\omega} d\omega. \quad (20)$$

This expression is equivalent to that used in Ref. [56], noting that in our convention the charge factor is already included in the definition of $S(\omega)$, whereas it is kept outside the strength function in Ref. [56].

III. RESULTS AND DISCUSSIONS

A. Properties of the initial ground state in AMD model

Before addressing the IVGDR, it is essential to assess the ground-state properties of ^{208}Pb predicted by the AMD model, including the binding energy per nucleon E_B/A , the charge radius r_{ch} , and the neutron skin thickness ΔR_{np} , in order to verify the reliability of the adopted interactions and the quality of the ground-state description.

As mentioned above, the cooling is stopped when the experimental binding energy is reached, or when the system reaches a local minimum with an energy higher than the experimental ground-state energy. This means that the calculated energy and density distributions of the initial ground state $|\Phi_0\rangle$ could be different event by event if the cooling is started from different states. In this work, we refer to this event-by-event difference of the ground state as the initial state fluctuation. In Fig. 1, as an example, we plot the density profiles of ^{208}Pb obtained with SLy4 and SkM* interactions. The thin lines are the results for 200 different initial ground states, and the thick lines are the 200 events averaged result.

Using the density distributions obtained for each event, the root-mean-square radii of protons and neutrons are calculated by removing the center-of-mass contribution,

$$\langle r_p^2 \rangle = \left\langle \frac{1}{Z} \sum_{i \in p} (\mathbf{r}_i - \mathbf{R}_{\text{cm}})^2 \right\rangle = \frac{1}{Z} \left\langle \sum_{i \in p} \mathbf{r}_i^2 \right\rangle - \langle \mathbf{R}_{\text{cm}}^2 \rangle,$$

$$\langle r_n^2 \rangle = \left\langle \frac{1}{N} \sum_{i \in n} (\mathbf{r}_i - \mathbf{R}_{\text{cm}})^2 \right\rangle = \frac{1}{N} \left\langle \sum_{i \in n} \mathbf{r}_i^2 \right\rangle - \langle \mathbf{R}_{\text{cm}}^2 \rangle, \quad (21)$$

where $\mathbf{R}_{\text{cm}} = \frac{1}{A} \sum_{i=1}^A \mathbf{r}_i$ is the center-of-mass coordinate of the nucleus, and then the charge radius and neutron skin thickness can be obtained as follows:

$$r_{ch} = \sqrt{\langle r_p^2 \rangle + (0.8 \text{ fm})^2}, \quad (22)$$

$$\Delta R_{np} = \langle r_n^2 \rangle^{1/2} - \langle r_p^2 \rangle^{1/2}.$$

One can expect that the E_B/A , r_{ch} , and ΔR_{np} are different from event to event, since the density distributions vary due to initial state fluctuations. In Table II, we list the values of $\langle E_B/A \rangle$, $\langle r_{ch} \rangle$, and $\langle \Delta R_{np} \rangle$, where the brackets $\langle \cdot \rangle$ means the ensemble average over 200 events. The standard deviations of these observables for 30 parameter sets depend on the effective interaction parameter sets. In general, the standard deviations of them are $\delta E_B/A < 0.01$ MeV, $\delta r_{ch} < 0.02$ fm, and $\delta \Delta R_{np} < 0.01$ fm.

Figs. 2 (a) and (b) show the dependence of $\langle \Delta R_{np} \rangle$ on S_0 and L . For a given value of L , $\langle \Delta R_{np} \rangle$ weakly depends on S_0 and $\Delta m_{np}^*/\delta = (m_n^* - m_p^*)/m$. In contrast, for a fixed S_0 , ΔR_{np} is strongly correlated to L , and $\langle \Delta R_{np} \rangle$ increases monotonically with the slope parameter L . This behavior is consistent with the well-known correlation that a stiffer symmetry energy leads to larger neutron skin. By comparing the calculated $\langle \Delta R_{np} \rangle$ with the PREX-II neutron skin data [57], we found only the sets with $L > 67$ MeV can reproduce the data.

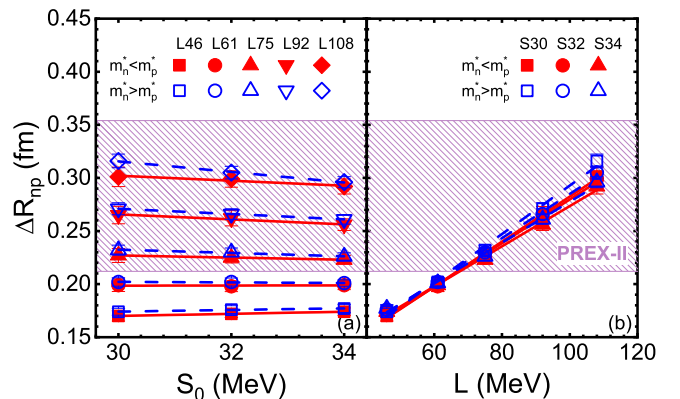


FIG. 2. The ΔR_{np} of ^{208}Pb as a function of S_0 (a), and L (b) for given 30 parameter sets.

TABLE II. The properties of ^{208}Pb in the AMD initial ground state for all 30 parameter sets. The experimental data are listed in the last row. S_0 , L , and E_B/A are in MeV; r_{ch} and ΔR_{np} are in fm. The symbols † and ‡ denote the SLy4 and SkM* interactions, respectively.

Sets	$\Delta m_{np}^*/\delta$ (f_I)	S_0	L	$\langle E_B/A \rangle$	$\langle r_{ch} \rangle$	$\langle \Delta R_{np} \rangle$
1			46	7.868	5.570	0.170
2			61	7.868	5.559	0.199
3	-0.15 (0.19)	30	75	7.868	5.548	0.227
4			92	7.869	5.534	0.265
5			108	7.869	5.521	0.301
6†			46	7.857	5.576	0.172
7			61	7.868	5.561	0.198
8	-0.15 (0.19)	32	75	7.868	5.549	0.225
9			92	7.868	5.536	0.262
10			108	7.869	5.520	0.299
11			46	7.818	5.584	0.174
12			61	7.843	5.568	0.199
13	-0.15 (0.19)	34	75	7.866	5.556	0.223
14			92	7.868	5.539	0.256
15			108	7.868	5.525	0.292
16‡			46	7.735	5.547	0.174
17			61	7.766	5.531	0.202
18	0.30 (-0.26)	30	75	7.801	5.518	0.232
19			92	7.848	5.494	0.271
20			108	7.868	5.472	0.316
21			46	7.700	5.552	0.176
22			61	7.728	5.537	0.202
23	0.30 (-0.26)	32	75	7.758	5.521	0.230
24			92	7.802	5.502	0.266
25			108	7.852	5.477	0.305
26			46	7.671	5.559	0.177
27			61	7.693	5.544	0.201
28	0.30 (-0.26)	34	75	7.720	5.529	0.226
29			92	7.761	5.505	0.261
30			108	7.805	5.486	0.296
Exp.				7.867	5.501 ± 0.001	0.283 ± 0.071 [21]

B. Time evolution of dipole moments and the transition strength function

To calculate the IVGDR within the AMD framework, we analyze the time evolution of the dipole moments of ^{208}Pb following an instantaneous electric dipole perturbation applied along the z direction.

In the present work, the perturbation strength is chosen as $\epsilon = 50 \text{ MeV } c^{-1} e^{-1}$. We have verified that the oscillation frequency of the induced dipole motion is independent of ϵ for $\epsilon \lesssim 72 \text{ MeV } c^{-1} e^{-1}$, ensuring that all calculations are performed within the linear response regime. Fig. 3 shows the time evolution of the dipole moment components $D_x(t)$, $D_y(t)$, and $D_z(t)$ for a representative event, where

$$D_i(t) = e \frac{NZ}{A} [R_{p,i}(t) - R_{n,i}(t)], \quad i = x, y, z. \quad (23)$$

The solid lines correspond to results obtained with the SLy4 interaction, while the dashed lines show those calculated with the SkM* interaction.

As shown in Figs. 3 (a) and (b), only weak fluctuations around zero are observed in both $D_x(t)$ and $D_y(t)$.

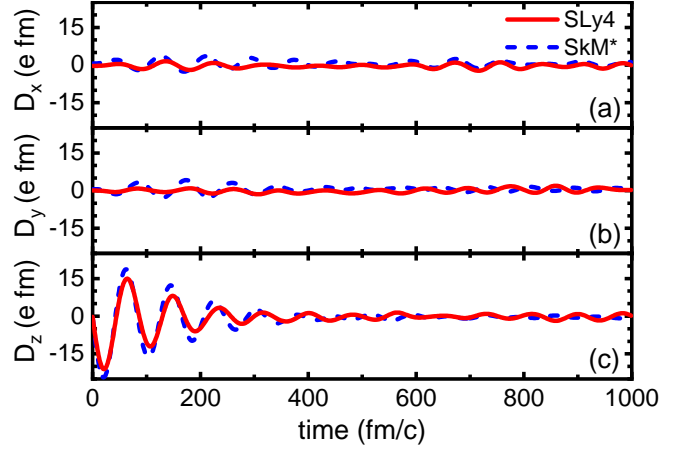


FIG. 3. The time evolution of the electric dipole moment in x , y , z directions for ^{208}Pb . Red lines are for SLy4, and blue lines are for SkM*.

These small amplitude components originate from the intrinsic inhomogeneity of the initial ground state density distributions. In contrast, a pronounced collective oscillation is clearly seen in the z component $D_z(t)$ [Fig. 3 (c)], which reflects the isovector dipole mode induced by the external perturbation. This oscillation is driven by the restoring force associated with the symmetry potential, which is mainly localized in the nuclear surface region.

The feature can be understood in a simple dynamical picture within the transport model, where the equation of motion of \mathbf{D} can be written as

$$\begin{aligned} \ddot{\mathbf{D}} = & e \frac{NZ}{Am} \nabla \left(\left(\frac{1}{m_s^*} - \frac{1}{m_v^*} \right) \hbar^2 k_F^2 \right) \frac{1}{2} \frac{\nabla \rho}{\rho} \cdot \mathbf{D} \\ & + e \frac{NZ}{Am} \left[\frac{2}{3} L(\rho) - 4S(\rho) \right] \frac{(\nabla \rho)^2}{\rho^2} \mathbf{D}. \end{aligned} \quad (24)$$

The derivation of above formula can be found in Appendix B. Thus, the oscillation frequency of the dipole mode can also be estimated from the force constant k by approximating the restoring force as $F \simeq -kD$. It means the oscillation frequency is proportional to the values of

$$e \frac{NZ}{Am} \left[4S(\rho) - \frac{2}{3} L(\rho) \right] \frac{(\nabla \rho)^2}{\rho^2}, \quad (25)$$

and

$$-e \frac{NZ}{Am} \left[\nabla \left(\left(\frac{1}{m_s^*} - \frac{1}{m_v^*} \right) \hbar^2 k_F^2 \right) \frac{1}{2} \frac{\nabla \rho}{\rho} \right]^T \quad (26)$$

at the surface of the nucleus as the gradient of the single particle potential approaches zero in the interior of the nucleus. The upper index T in Eq.(26) means the transpose of matrix in bracket $[\cdot]$. Formally, the frequency depends on the isovector effective mass $m_v^*(\rho)$, isoscalar effective mass $m_s^*(\rho)$, the slope of symmetry energy $L(\rho)$ and the strength of symmetry energy $S(\rho)$.

According to Eq. (25), a larger value of S_0 yields a larger symmetry energy over the entire density range

compared to a smaller S_0 , which implies a stronger restoring force and thus a higher oscillation frequency (or equivalently, a higher centroid energy) for larger S_0 . However, the centroid energy for a larger L is smaller than that for a smaller L . This is because a stiffer symmetry energy corresponds to a smaller symmetry energy at subsaturation densities compared with a softer symmetry energy. Consequently, a larger L leads to a smaller centroid energy. The difference between the isoscalar effective mass and isovector effective mass, i.e., $f_I = m/m_s^* - m/m_v^*$, also affects the main frequency of the strength function. The positive value of f_I will decrease the frequency, whereas the negative value of f_I will increase the frequency.

As shown in Fig. 3, the amplitude of the oscillation gradually decreases over time due to the Landau damping mechanism. This mechanism means that the different local mean fields and effective masses experienced by individual Gaussian wave packets lead to different oscillation frequencies, and this phase-mixing mechanism leads to a gradual loss of phase coherence. This picture appears different from that in the RPA framework, where Landau damping originates from the fragmentation of the collective strength over particle-hole configurations in energy space.

By using Eqs. (16)-(19), the strength function $S(E)$ can be obtained for each event. Due to the presence of initial ground-state fluctuations in the AMD calculations, the different events yield different $S(E)$ as illustrated in Fig. 4 (thin lines). To compare the calculations to data, the event-averaged $S(E)$ is calculated over 200 events. To measure the uncertainty caused by this fluctuation, the standard deviation of $S(E)$ is also calculated. The event-averaged $S(E)$ (thick lines) and its corresponding standard deviations are presented in Fig. 4. The event-averaged $S(E)$ with SLy4 effective interaction is close to the data (black points) without introducing the smoothing parameter Γ as in Ref. [55] owing to the Landau damping, although adding a width of 1 MeV can further improve the agreement with the data. The above mechanism is different than the discussions in the BUU transport models in Refs. [32, 45–47], in which two-body collisions also contribute to the spreading the strength function. The spurious two-body collisions are caused by the underestimations of the Pauli blocking probability in the BUU type models [50]. In addition, we also turn on the nucleon-nucleon collisions in the AMD model to check its influence on $S(E)$, and our calculations show that the difference of the integration of $S(E)$ is less than 0.47% due to the well describe Pauli blocking in AMD model.

C. Influence of S_0 , L and f_I on $S(E)$

Before constraining the symmetry energy via the IVGDR, we first examine the strength function $S(E)$ obtained with two typical effective interactions, i.e., SLy4

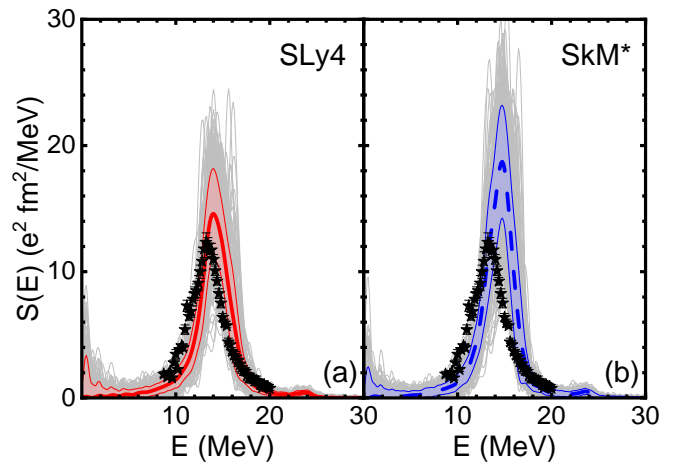


FIG. 4. Isovector giant dipole resonance strength function for ^{208}Pb . Thin lines are the results obtained by AMD with 200 events, and thick lines are the event averaged values. Left panel is for SLy4, and right panel is for SkM*.

and SkM*. Both interactions have the same L , but different S_0 values and isoscalar and isovector effective mass (or different f_I) [12, 58]. Fig. 4(a) shows the results obtained with the SLy4 interaction, while panel (b) corresponds to SkM*. Our calculations show that the SLy4 effective interaction ($f_I = 0.19$, i.e., $m_n^* < m_p^*$) has a smaller centroid energy of $S(E)$ than that with SkM* ($f_I = -0.26$, i.e., $m_n^* > m_p^*$). The centroid energy of $S(E)$ obtained with SLy4 is about 14.0 MeV, which is lower than that obtained with SkM* (about 14.7 MeV). This difference between mainly comes from the impact of f_I .

To illustrate the influence of S_0 , L , and f_I on $S(E)$, we performed calculations with 30 parameter sets featuring different values of f_I , S_0 , and L , as summarized in Table I, and the results are presented in Fig. 5. The left panels in Fig. 5 show the $S(E)$ for 1-15 sets with $f_I = 0.19$ ($m_n^* < m_p^*$), while the right panels correspond to the results for 16-30 sets with $f_I = -0.26$ ($m_n^* > m_p^*$). The panels from top to bottom correspond to $S_0 = 30$, 32, and 34 MeV, respectively. The lines in each panel represent the results obtained with different values of L . Our calculations clearly demonstrate that the centroid energies increase with increasing S_0 and decrease with increasing L , with all other parameters fixed. In addition, the centroid energy is systematically larger for $f_I < 0$ ($\Delta m_{np}^* > 0$) than for $f_I > 0$ ($\Delta m_{np}^* < 0$) at a given S_0 and L .

To quantitatively assess the agreement between the theoretical calculations and the experimental data, we performed a χ^2 analysis for all 30 parameter sets. The reduced χ_r^2 is defined as

$$\chi_r^2 = \frac{1}{N_{\text{exp}}} \sum_{i=1}^{N_{\text{exp}}} \frac{[S_{\text{th}}(E_i) - S_{\text{exp}}(E_i)]^2}{\sigma_{\text{th}}^2(E_i) + \sigma_{\text{exp}}^2(E_i)}, \quad (27)$$

where $S_{\text{th}}(E_i)$ and $S_{\text{exp}}(E_i)$ denote the theoretical and

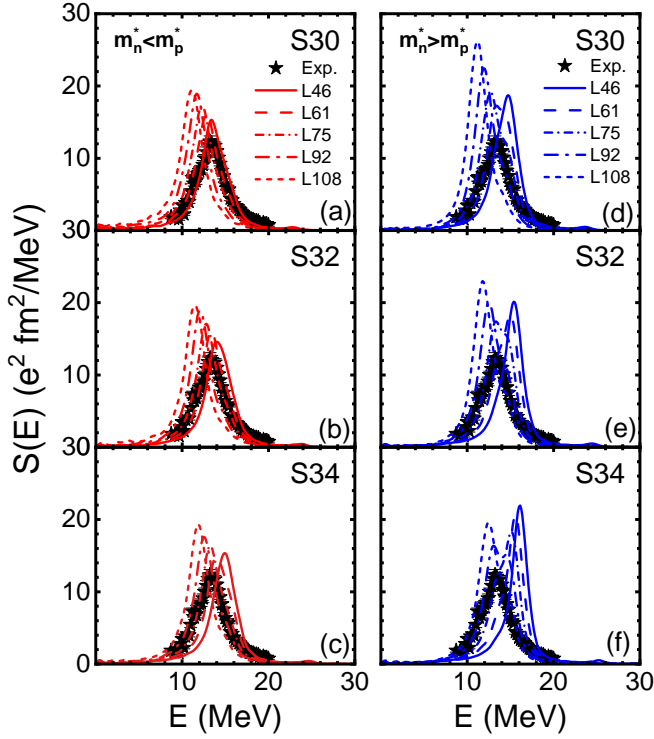


FIG. 5. Calculated IVGDR strength functions and data for ^{208}Pb .

TABLE III. The calculated χ_r^2 values for all 30 parameter sets compared with the experimental data.

Sets	$\Delta m_{np}^*/\delta (f_I)$	S_0 (MeV)	L (MeV)	χ_r^2
1		46	16.15	
2		61	14.17	
3	-0.15 (0.19)	30	75	60.78
4		92	159.23	
5		108	289.66	
6		46	55.70	
7		61	15.45	
8	-0.15 (0.19)	32	75	17.13
9		92	95.14	
10		108	223.21	
11		46	127.51	
12		61	59.41	
13	-0.15 (0.19)	34	75	14.21
14		92	27.62	
15		108	126.94	
16		46	115.75	
17		61	47.14	
18	0.30 (-0.26)	30	75	36.15
19		92	124.21	
20		108	335.22	
21		46	189.99	
22		61	117.80	
23	0.30 (-0.26)	32	75	49.76
24		92	49.94	
25		108	148.10	
26		46	249.13	
27		61	190.39	
28	0.30 (-0.26)	34	75	126.59
29		92	46.59	
30		108	52.93	

experimental $E1$ strength function at energy E_i , respectively, $\sigma_{\text{exp}}(E_i)$ is the experimental uncertainty and $\sigma_{\text{th}}(E_i)$ represents the statistical uncertainty of the theoretical mean at energy E_i . N_{exp} corresponds to the number of experimental data points. The detailed results are summarized in Table III. Our calculations show that the parameter set with $f_I = 0.19$, $S_0 = 30$ MeV, and $L = 61$ MeV can describe the data with $\chi_r^2 = 14.17$. It means that an accurate description of $S(E)$ still needs more work.

D. Constraining symmetry energy via α_D and ΔR_{np}

To understand the tension on the constraints of symmetry energy from α_D and ΔR_{np} appeared in the density functional theory [33], we perform the following combination analysis within the framework of AMD model.

Figs. 6 (a) and (b) display the electric dipole polarizability α_D as a function of S_0 and L , respectively. Similarly to the neutron skin, α_D exhibits a robust linear dependence on L . However, in contrast to the neutron skin thickness, the α_D also shows a pronounced dependence on S_0 and Δm_{np}^* . Specifically, for a fixed L , the sets with $\Delta m_{np}^* > 0$ (blue lines) yields systematically higher α_D values than the sets with $\Delta m_{np}^* < 0$ (red lines), consistent with the results reported in Ref. [45]. By comparing the calculations to the α_D data [41, 59], we found that the sets with $S_0 = [30, 34]$ and $L = [43, 75]$ are compatible with the data within the uncertainties. Moreover, the extracted S_0 is positively correlated with L .

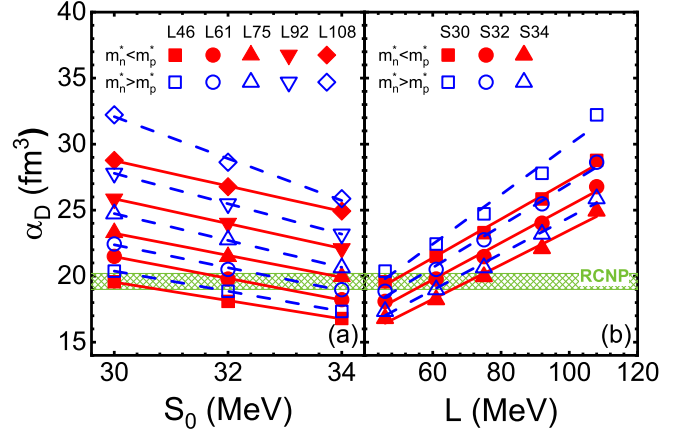


FIG. 6. The α_D of ^{208}Pb as a function of S_0 (a), and L (b) for given 30 parameter sets.

To extract the favored effective interactions by simultaneously describing both ΔR_{np} and α_D , we present ΔR_{np} as a function of α_D in Fig. 7. A clear linear correlation between these two observables is observed when L is varied keeping S_0 and the effective mass splitting fixed, in agreement with the findings of Ref. [39]. Our calculations indicate that a simultaneous reproduction of ΔR_{np} and α_D favors relatively larger values of the

symmetry energy at saturation, i.e., $S_0 \simeq 34$ MeV in the present analysis, and the favored $L \simeq 67$ – 75 MeV for $f_I = 0.19$ ($\Delta m_{np}^* < 0$) and $L \simeq 66$ – 69 MeV for $f_I = -0.26$ ($\Delta m_{np}^* > 0$). It should be emphasized that α_D is predominantly sensitive to the symmetry energy at subsaturation densities, which means the parameters S_0 and L are the uncontrolled extrapolated results.

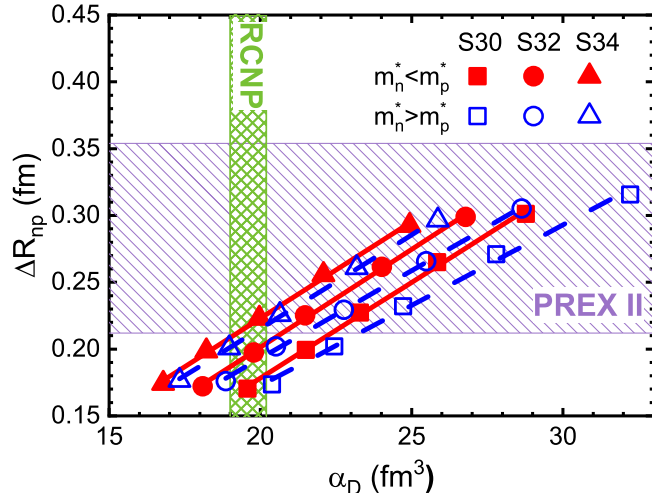


FIG. 7. Correlation between the neutron skin thickness ΔR_{np} and the electric dipole polarizability α_D for ^{208}Pb .

It is therefore crucial to identify the density region to which the observables α_D and ΔR_{np} are most sensitive, and to extract the symmetry energy at the corresponding densities. Following the same procedure as in Ref. [30], we evaluate the Pearson correlation coefficient between the inverse dipole polarizability $1/\alpha_D$ and the symmetry energy $S(\rho)$. We find that the correlation coefficient exceeds 0.99 over the subsaturation density interval $0.20 \leq \rho/\rho_0 \leq 0.57$. This strong correlation demonstrates that the IVGDR predominantly probes the symmetry energy in this specific density region. The constraint imposed solely by the RCNP α_D data is depicted by the purple region in Fig. 8. The constraint imposed simultaneously by the RCNP α_D and the PREX-II neutron skin data is depicted by the red region in Fig. 8. Quantitatively, we obtain a tightly constrained symmetry energy of $S(\rho) = 10.5 \pm 0.63$ MeV at $\rho/\rho_0 = 0.20$, and $S(\rho) = 23.1 \pm 0.40$ MeV at $\rho/\rho_0 = 0.57$.

To provide a comprehensive comparison of symmetry-energy constraints at their respective sensitive densities, we present in Fig. 8 a summary plot similar to that in Ref. [60]. Various isospin-sensitive observables that have been used to constrain the symmetry energy at subsaturation densities are included for comparison. For instance, analyses of electric dipole polarizability with RPA method [49, 60] provide constraints around $\rho/\rho_0 \approx 1/3$, yielding $S(\rho_0/3) = 16.4$ – 17.8 MeV. The purple left-pointing triangle denotes the constraint extracted from the neutron-proton Fermi-energy difference at a subsaturation density of $\rho \simeq 0.11$ fm $^{-3}$, giving

$S(\rho) = 26.2 \pm 1.0$ MeV [61]. The dark-gray right-pointing triangle corresponds to the constraint deduced from binding energy differences between heavy isotope pairs, which yields $S(\rho_c) = 26.65 \pm 0.20$ MeV at $\rho_c \approx 0.11$ fm $^{-3}$ [23]. The isospin diffusion in HICs [9, 10, 62] constrains the symmetry energy at $\rho/\rho_0 = 0.21 \pm 0.11$ with $S(\rho) = 10.1 \pm 1.0$ MeV. The single and double neutron-proton yield ratios constrain the symmetry energy near $\rho/\rho_0 \approx 0.43$ with $S(\rho) = 16.8 \pm 1.2$ MeV [63]. Our extracted constraints on the symmetry energy in the sensitive density region $0.20 \leq \rho/\rho_0 \leq 0.57$ are consistent with those constraints via different approaches within uncertainties. Furthermore, our constraints on symmetry energy also fall into the predicted region of the symmetry energy by using chiral effective field theory [64, 65]. This overall agreement supports the robustness of the symmetry energy constraints in this density domain.

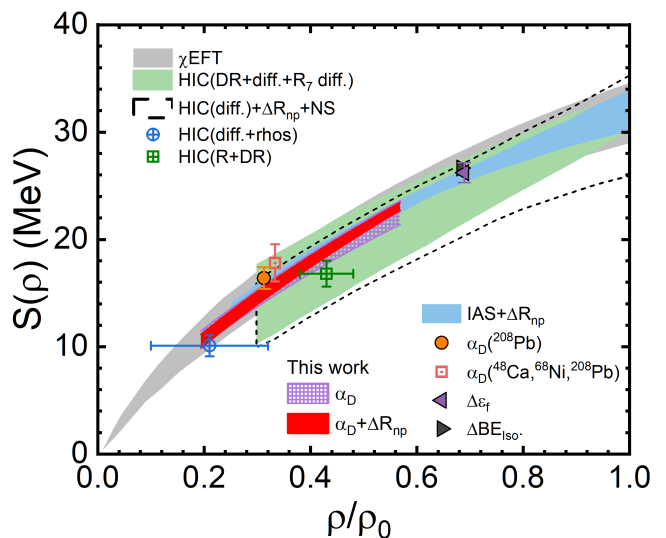


FIG. 8. Constraints on the symmetry energy $S(\rho)$ as a function of normalized density ρ/ρ_0 .

IV. SUMMARY

In this work, we investigated the isovector giant dipole resonance and the neutron skin properties of ^{208}Pb within the framework of the antisymmetrized molecular dynamics model. Our calculations show that the AMD model can naturally reproduce the strength function distribution $S(E)$ even without introducing additional smoothing parameters and two-body nucleon-nucleon collisions. This behavior can be attributed to an intrinsic Landau damping mechanism in the transport models, in which the different local mean fields and effective masses experienced by individual Gaussian wave packets lead to different oscillation frequencies, and this phase-mixing mechanism leads to a gradual loss of phase coherence.

Furthermore, our calculations show that the main fre-

quency of IVGDR is dominated by the symmetry potential at the surface of the nucleus. The main frequency of IVGDR increases with the symmetry energy coefficient S_0 and the strength of nucleon effective mass splitting Δm_{np}^* , but decreases with L due to the symmetry energy increasing with L decreasing at subsaturation density. As a consequence of $S(E)$ -weighted integral observable, the electric dipole polarizability α_D depends on S_0 , L , and Δm_{np}^* . In addition, the density profile and neutron skin of ^{208}Pb can also be well described by AMD model with certain effective interaction parameters. The neutron skin thickness ΔR_{np} is strongly sensitive to the slope of symmetry energy but weakly sensitive to the symmetry energy coefficient S_0 and nucleon effective mass splitting Δm_{np}^* .

By performing a combined analysis of ΔR_{np} and α_D within the unified AMD framework, we have extracted favored symmetry energy parameters that simultaneously reproduce the PREX-II neutron skin and RCNP dipole polarizability data. The combined constraints favor a relatively large symmetry energy at saturation, $S_0 \simeq 34$ MeV, and a slope parameter in the range $L \simeq 66$ – 75 MeV, with only a weak dependence on the effective mass splitting. Furthermore, a correlation analysis reveals that the IVGDR predominantly probes the symmetry energy in the subsaturation density window $0.20 \leq \rho/\rho_0 \leq 0.57$. Within this region, we extract tight constraints on the density dependence of the symmetry energy, yielding $S(\rho) = 10.5 \pm 0.63$ MeV at $\rho/\rho_0 = 0.20$ and $S(\rho) = 23.1 \pm 0.4$ MeV at $\rho/\rho_0 = 0.57$.

Nevertheless, the accurate description of $S(E)$ favors the parameter set with $S_0 = 30$ MeV and $L = 61$ MeV, which seems different from the combination analysis with α_D and ΔR_{np} . This difference indicates that a full quantitative description of the IVGDR strength function may require an extended exploration of the interaction parameter space and possibly additional dynamical ingredients.

ACKNOWLEDGMENTS

This work was supported by the National Natural Science Foundation of China under Grants No. 12275359, No. 12375129, No. 11875323 and No. 11961141003, by JSPS KAKENHI Grant No. JP21K03528, by the National Key R&D Program of China under Grant No. 2023 YFA1606402, by the Continuous Basic Scientific Research Project, by funding of the China Institute of Atomic Energy under Grant No. YZ222407001301, No. YZ232604001601, No. YC010270525794 and No. PA010271225779, and by the Leading Innovation Project of the CNCN under Grants No. LC192209000701 and No. LC202309000201. We acknowledge support by the computing server SCATP in China Institute of Atomic Energy.

DATA AVAILABILITY

The data that support the findings of this article are not publicly available upon publication because it is not technically feasible and/or the cost of preparing, depositing, and hosting the data would be prohibitive within the terms of this research project. The data are available from the authors upon reasonable request.

Appendix A: Details of Parameter Sets

In this Appendix, we list the detailed values of the parameter sets used in our calculations.

TABLE IV. The parameter sets (S_0 , L) and corresponding coupling constants (x_3 , x'_3) used in the calculations.

Sets	m_s^*	m_v^*	S_0 (MeV)	L (MeV)	x_3	x'_3
1			46		1.18	
2			61		0.73	
3	0.695	0.800	30	75	1.383	0.32
4			92		-0.19	
5			108		-0.66	
6			46		0.00	
7			61		0.91	
8	0.695	0.800	32	75	1.354	0.50
9			92		-0.01	
10			108		-0.50	
11			46		1.53	
12			61		1.09	
13	0.695	0.800	34	75	1.324	0.66
14			92		0.17	
15			108		-0.32	
16			46		0.00	
17			61		-0.39	
18	0.789	0.653	30	75	0.000	-0.77
19			92		-1.20	
20			108		-1.63	
21			46		0.147	
22			61		-0.25	
23	0.789	0.653	32	75	-0.026	-0.61
24			92		-1.05	
25			108		-1.47	
26			46		0.30	
27			61		-0.09	
28	0.789	0.653	34	75	-0.052	-0.45
29			92		-0.90	
30			108		-1.31	

Appendix B: Motion of dipole moment

The dipole moment \mathbf{D} is defined as the difference between the center-of-mass of protons and neutrons, i.e.,

$$\begin{aligned}\mathbf{D} &\equiv e \frac{NZ}{A} (\mathbf{R}_p(t) - \mathbf{R}_n(t)) \\ &= e \frac{NZ}{A} \left(\frac{1}{Z} \sum_{i \in p} \mathbf{r}_i - \frac{1}{N} \sum_{i \in n} \mathbf{r}_i \right).\end{aligned}\quad (\text{B1})$$

When a spherical nucleus is not perturbed by the dipole electric field, we will have $\mathbf{D} = 0$. Under the dipole perturbation, $\mathbf{D} \neq 0$. If we move all neutrons (protons) with the same values, i.e., $\mathbf{r}_i \rightarrow \mathbf{r}_i - \mathbf{D}_n$ for neutrons and $\mathbf{r}_i \rightarrow \mathbf{r}_i - \mathbf{D}_p$ for protons, we will have $\mathbf{D} = \mathbf{D}_p - \mathbf{D}_n$.

Here we assume a Goldhaber-Teller-like mode, where proton and neutron densities undergo small rigid displacements. To linear order in the dipole coordinate, the local isospin asymmetry can be written as

$$\begin{aligned}\rho_n(\mathbf{r}_i) &\rightarrow \rho_n(\mathbf{r}_i - \mathbf{D}_n) \approx \rho_n(\mathbf{r}) - \nabla \rho_n \cdot \mathbf{D}_n, \\ \rho_p(\mathbf{r}_i) &\rightarrow \rho_p(\mathbf{r}_i - \mathbf{D}_p) \approx \rho_p(\mathbf{r}) - \nabla \rho_p \cdot \mathbf{D}_p.\end{aligned}\quad (\text{B2})$$

Usually, the δ of the nucleus is relatively small and it means that we can approximately describe $\rho_n \approx \rho_p \approx \rho/2$. Thus, the total density remained almost constant because

$$\rho_n(\mathbf{r}_i) + \rho_p(\mathbf{r}_i) \approx \rho_n(\mathbf{r}_i - \mathbf{D}_n) + \rho_p(\mathbf{r}_i - \mathbf{D}_p) = \rho(\mathbf{r}).\quad (\text{B3})$$

In the above derivation, we also use the condition that $(\mathbf{D}_n + \mathbf{D}_p) = 0$. Another, the difference between the neutron and proton densities becomes,

$$\rho_n(\mathbf{r}_i) - \rho_p(\mathbf{r}_i) \approx \frac{1}{2} \nabla \rho \cdot \mathbf{D}.\quad (\text{B4})$$

It means that the isospin asymmetry can be expressed as

$$\delta(\mathbf{r}_i) \approx \frac{1}{2} \frac{\nabla \rho}{\rho} \cdot \mathbf{D}\quad (\text{B5})$$

and δ will give a contribution of \mathbf{D} in the expression of the mean field.

Now, let's to see how the \mathbf{D} evolves. Based on the single particle potential of the neutron and proton, the second order time derivative of \mathbf{D} becomes,

$$\begin{aligned}\ddot{\mathbf{D}} &= e \frac{NZ}{A} \left(\frac{1}{Z} \sum_{i \in p} \ddot{x}_i - \frac{1}{N} \sum_{i \in n} \ddot{x}_i \right) \\ &= e \frac{NZ}{A} \left(\frac{1}{Zm} \sum_{i \in p} m \ddot{x}_i - \frac{1}{Nm} \sum_{i \in n} m \ddot{x}_i \right) \\ &= e \frac{NZ}{A} \left(\frac{1}{Zm} \sum_{i \in p} (-\nabla_i \epsilon_p) - \frac{1}{Nm} \sum_{i \in n} (-\nabla_i \epsilon_n) \right)\end{aligned}\quad (\text{B6})$$

Here, ϵ_n and ϵ_p are the single particle energy, which consists of the single particle potential of the neutron and proton, i.e., U_n and U_p , and the single particle kinetic energy, ϵ_k^n and ϵ_k^p .

$$\begin{aligned}\epsilon_n &= \frac{p^2}{2m_n^*} + U_n^{loc} \approx \frac{p_{F,n}^2}{2m_n^*} + U_0^{loc} + U_{sym}^{loc} \delta, \\ \epsilon_p &= \frac{p^2}{2m_p^*} + U_p^{loc} \approx \frac{p_{F,p}^2}{2m_p^*} + U_0^{loc} - U_{sym}^{loc} \delta.\end{aligned}\quad (\text{B7})$$

U_0^{loc} and U_{sym}^{loc} mean that the potential arises from the local interactions for symmetric and asymmetric part, respectively. The nonlocal interactions are involved into the effective kinetic energy terms.

By inserting the above formula into Eq. (B6) and supposing that each nucleon feels the same single particle potential, we will have

$$\begin{aligned}\ddot{\mathbf{D}} &= -e \frac{NZ}{Am} (\nabla \epsilon_p - \nabla \epsilon_n) \\ &\approx e \frac{NZ}{Am} \nabla \left(\frac{p_{F,n}^2}{2m_n^*} - \frac{p_{F,p}^2}{2m_p^*} + 2U_{sym}^{loc} \delta \right) \\ &= e \frac{NZ}{Am} \nabla \left(\left(\frac{\hbar^2}{2m_n^*} - \frac{\hbar^2}{2m_p^*} \right) k_F^2 \right. \\ &\quad \left. + \frac{2}{3} \left(\frac{\hbar^2}{2m_n^*} + \frac{\hbar^2}{2m_p^*} \right) k_F^2 \delta + 2U_{sym}^{loc} \delta \right) \\ &= e \frac{NZ}{Am} \nabla \left(\left(\frac{1}{m_s^*} - \frac{1}{m_v^*} \right) \hbar^2 k_F^2 \delta + \frac{4}{3} \frac{\hbar^2}{2m_s^*} k_F^2 \delta + 2U_{sym}^{loc} \delta \right) \\ &= e \frac{NZ}{Am} \nabla \left(\left(\frac{1}{m_s^*} - \frac{1}{m_v^*} \right) \hbar^2 k_F^2 \delta + 4S(\rho) \delta \right)\end{aligned}\quad (\text{B8})$$

In the above derivations, the following relationship is used. 1), The Laplacian term $\nabla^2 \rho$ is approximately expressed in terms of $(\nabla \rho)^2 / \rho$ in the nuclear surface region, where the density exhibits a Fermi-type profile. 2), The $\frac{1}{m_n^*} \frac{1}{m_p^*} \approx \frac{1}{m_s^{*2}}$ is used according to the relationship in Ref. [66]. 3), the density dependence of symmetry energy can be expressed as [67],

$$S(\rho) = \frac{1}{3} \frac{\hbar^2 k_F^2}{2m_N^*} + \frac{1}{2} U_{sym}^{loc}.\quad (\text{B9})$$

Thus, we can rewrite the $\ddot{\mathbf{D}}$ as

$$\begin{aligned}
\ddot{\mathbf{D}} &= e \frac{NZ}{Am} \nabla \left(\left(\frac{1}{m_s^*} - \frac{1}{m_v^*} \right) \hbar^2 k_F^2 \delta + 4S(\rho) \delta \right) \\
&= e \frac{NZ}{Am} \nabla \left(\left(\frac{1}{m_s^*} - \frac{1}{m_v^*} \right) \hbar^2 k_F^2 \frac{1}{2} \frac{\nabla \rho}{\rho} \cdot \mathbf{D} + 4S(\rho) \frac{1}{2} \frac{\nabla \rho}{\rho} \cdot \mathbf{D} \right) \\
&\approx e \frac{NZ}{Am} \nabla \left(\left(\frac{1}{m_s^*} - \frac{1}{m_v^*} \right) \hbar^2 k_F^2 \right) \frac{1}{2} \frac{\nabla \rho}{\rho} \cdot \mathbf{D} \\
&\quad + e \frac{NZ}{Am} \left[2 \nabla S(\rho) \cdot \frac{\nabla \rho}{\rho} + 2S(\rho) \left(-\frac{(\nabla \rho)^2}{\rho^2} + \frac{\nabla^2 \rho}{\rho} \right) \right] \cdot \mathbf{D} \\
&= e \frac{NZ}{Am} \nabla \left(\left(\frac{1}{m_s^*} - \frac{1}{m_v^*} \right) \hbar^2 k_F^2 \right) \frac{1}{2} \frac{\nabla \rho}{\rho} \cdot \mathbf{D} \\
&\quad + e \frac{NZ}{Am} \left[2 \frac{\partial S(\rho)}{\partial \rho} \frac{(\nabla \rho)^2}{\rho} + 2S(\rho) \left(-2 \frac{(\nabla \rho)^2}{\rho^2} \right) \right] \cdot \mathbf{D} \\
&= e \frac{NZ}{Am} \nabla \left(\left(\frac{1}{m_s^*} - \frac{1}{m_v^*} \right) \hbar^2 k_F^2 \right) \frac{1}{2} \frac{\nabla \rho}{\rho} \cdot \mathbf{D} \\
&\quad + e \frac{NZ}{Am} \left[\frac{2}{3} L(\rho) - 4S(\rho) \right] \frac{(\nabla \rho)^2}{\rho^2} \mathbf{D}
\end{aligned} \tag{B10}$$

It means the oscillation frequency will depend on the values of isoscalar effective mass, isovector effective mass, the slope of symmetry energy and the strength of symmetry energy at subsaturation density as the gradient term vanishes at the inner of nucleus.

To isolate the \mathbf{D} in the first term of Eq.(B10), we rewritten it as,

$$\begin{aligned}
&e \frac{NZ}{Am} \nabla \left(\left(\frac{1}{m_s^*} - \frac{1}{m_v^*} \right) \hbar^2 k_F^2 \right) \frac{1}{2} \frac{\nabla \rho}{\rho} \cdot \mathbf{D} \\
&= e \frac{NZ}{Am} \left[\nabla \left(\left(\frac{1}{m_s^*} - \frac{1}{m_v^*} \right) \hbar^2 k_F^2 \frac{1}{2} \frac{\nabla \rho}{\rho} \right) \right]^T \mathbf{D}.
\end{aligned} \tag{B11}$$

It means that the frequency of IVGDR is also influenced by the isoscalar and isovector effective mass.

-
- [1] NuPECC Long Range Plan 2024 for European Nuclear Physics (2025), [arXiv:2503.15575](https://arxiv.org/abs/2503.15575) [nucl-ex].
- [2] US Department of Energy (USDOE), *A New Era of Discovery: The 2023 Long Range Plan for Nuclear Science*, Tech. Rep. (US Department of Energy (USDOE), 2023).
- [3] M. B. Tsang, J. R. Stone, F. Camera, P. Danielewicz, S. Gandolfi, K. Hebeler, C. J. Horowitz, J. Lee, W. G. Lynch, Z. Kohley, R. Lemmon, P. Möller, T. Murakami, S. Riordan, X. Roca-Maza, F. Sammarruca, A. W. Steiner, I. Vidaña, and S. J. Yennello, Constraints on the symmetry energy and neutron skins from experiments and theory, *Phys. Rev. C* **86**, 015803 (2012).
- [4] B.-A. Li, B.-J. Cai, W.-J. Xie, and N.-B. Zhang, Progress in constraining nuclear symmetry energy using neutron star observables since gw170817, *Universe* **7**, 182 (2021).
- [5] G. Burgio, H.-J. Schulze, I. Vidaña, and J.-B. Wei, Neutron stars and the nuclear equation of state, *Progress in Particle and Nuclear Physics* **120**, 103879 (2021).
- [6] C. Y. Tsang, M. B. Tsang, W. G. Lynch, R. Kumar, and C. J. Horowitz, Determination of the equation of state from nuclear experiments and neutron star observations, *Nature Astronomy* **8**, 328336 (2024).
- [7] J. M. Lattimer and A. W. Steiner, Constraints on the symmetry energy using the mass-radius relation of neutron stars, *The European Physical Journal A* **50**, 10.1140/epja/i2014-14040-y (2014).
- [8] N.-B. Zhang, B.-A. Li, and J. Xu, Combined constraints on the equation of state of dense neutron-rich matter from terrestrial nuclear experiments and observations of neutron stars, *The Astrophysical Journal* **859**, 90 (2018).
- [9] Y. Zhang, M. Liu, C.-J. Xia, Z. Li, and S. K. Biswal, Constraints on the symmetry energy and its associated parameters from nuclei to neutron stars, *Phys. Rev. C* **101**, 034303 (2020).
- [10] M. B. Tsang, Y. Zhang, P. Danielewicz, M. Famiano, Z. Li, W. G. Lynch, and A. W. Steiner, Constraints on the density dependence of the symmetry energy, *Phys. Rev. Lett.* **102**, 122701 (2009).
- [11] L.-W. Chen, C. M. Ko, and B.-A. Li, Determination of the stiffness of the nuclear symmetry energy from isospin diffusion, *Phys. Rev. Lett.* **94**, 032701 (2005).
- [12] Y. Zhang, M. Tsang, Z. Li, and H. Liu, Constraints on nucleon effective mass splitting with heavy ion collisions, *Physics Letters B* **732**, 186 (2014).
- [13] B.-A. Li, L.-W. Chen, and C. M. Ko, Recent progress and new challenges in isospin physics with heavy-ion reactions, *Physics Reports* **464**, 113 (2008).
- [14] M. A. Famiano, T. Liu, W. G. Lynch, M. Mocko, A. M. Rogers, M. B. Tsang, M. S. Wallace, R. J. Charity, S. Komarov, D. G. Sarantites, L. G. Sobotka, and G. Verde, Neutron and proton transverse emission ratio measurements and the density dependence of the asymmetry term of the nuclear equation of state, *Phys. Rev. Lett.* **97**, 052701 (2006).
- [15] J. Yang, Y. Zhang, N. Wang, and Z. Li, Influence of the treatment of initialization and mean-field potential on the neutron to proton yield ratios, *Phys. Rev. C* **104**, 024605 (2021).
- [16] Z. Y. Sun, M. B. Tsang, W. G. Lynch, G. Verde, F. Amorini, L. Andronenko, M. Andronenko, G. Cardella, M. Chatterje, P. Danielewicz, E. De Filippo, P. Dinh, E. Galichet, E. Geraci, H. Hua, E. La Guidara, G. Lanzalone, H. Liu, F. Lu, S. Lukyanov, C. Maiolino, A. Pagano, S. Piantelli, M. Papa, S. Pirrone, G. Politi, F. Porto, F. Rizzo, P. Russotto, D. Santonocito, and Y. X. Zhang, Isospin diffusion and equilibration for Sn + Sn collisions at $e/a = 35$ mev, *Phys. Rev. C* **82**, 051603 (2010).
- [17] C. Ciampi, J. D. Frankland, D. Gruyer, N. Le Neindre,

- S. Mallik, R. Bougault, A. Chbihi, L. Baldesi, S. Barlini, E. Bonnet, B. Borderie, A. Camaiani, G. Casini, I. Dekhissi, D. Dell'Aquila, J. A. Dueñas, Q. Fable, F. Gramegna, C. Gouyet, M. Henri, B. Hong, S. Kim, A. Kordyasz, T. Kozik, M. J. Kweon, I. Lombardo, O. Lopez, L. Manduci, T. Marchi, K. Mazurek, S. H. Nam, J. Park, M. Pârlog, G. Pasquali, S. Piantelli, G. Poggi, A. Rebillard-Soulié, R. Revenko, S. Valdré, G. Verde, and E. Vient (INDRA-FAZIA Collaboration), Model-independent measurement of isospin diffusion in ni-ni systems at intermediate energy, *Phys. Rev. C* **111**, 044601 (2025).
- [18] Z. Xiao, B.-A. Li, L.-W. Chen, G.-C. Yong, and M. Zhang, Circumstantial evidence for a soft nuclear symmetry energy at suprasaturation densities, *Physical Review Letters* **102**, 10.1103/physrevlett.102.062502 (2009).
- [19] M. Cozma, The impact of energy conservation in transport models on the ν multiplicity ratio in heavy-ion collisions and the symmetry energy, *Physics Letters B* **753**, 166 (2016).
- [20] Y. Liu, Y. Wang, Y. Cui, C.-J. Xia, Z. Li, Y. Chen, Q. Li, and Y. Zhang, Insights into the pion production mechanism and the symmetry energy at high density, *Phys. Rev. C* **103**, 014616 (2021).
- [21] B. T. Reed, F. J. Fattoyev, C. J. Horowitz, and J. Piekarewicz, Implications of prex-2 on the equation of state of neutron-rich matter, *Phys. Rev. Lett.* **126**, 172503 (2021).
- [22] X. Roca-Maza, M. Centelles, X. Viñas, and M. Warda, Neutron skin of ^{208}Pb , nuclear symmetry energy, and the parity radius experiment, *Phys. Rev. Lett.* **106**, 252501 (2011).
- [23] Z. Zhang and L.-W. Chen, Constraining the symmetry energy at subsaturation densities using isotope binding energy difference and neutron skin thickness, *Physics Letters B* **726**, 234238 (2013).
- [24] M. Centelles, X. Roca-Maza, X. Viñas, and M. Warda, Nuclear symmetry energy probed by neutron skin thickness of nuclei, *Phys. Rev. Lett.* **102**, 122502 (2009).
- [25] T.-G. Yue, L.-W. Chen, Z. Zhang, and Y. Zhou, Constraints on the symmetry energy from prex-ii in the multimessenger era, *Phys. Rev. Res.* **4**, L022054 (2022).
- [26] X. Roca-Maza and N. Paar, Nuclear equation of state from ground and collective excited state properties of nuclei, *Progress in Particle and Nuclear Physics* **101**, 96 (2018).
- [27] L. Trippa, G. Colò, and E. Vigezzi, Giant dipole resonance as a quantitative constraint on the symmetry energy, *Phys. Rev. C* **77**, 061304 (2008).
- [28] X. Roca-Maza, M. Brenna, G. Colò, M. Centelles, X. Viñas, B. K. Agrawal, N. Paar, D. Vretenar, and J. Piekarewicz, Electric dipole polarizability in ^{208}pb : Insights from the droplet model, *Phys. Rev. C* **88**, 024316 (2013).
- [29] G. Colò, U. Garg, and H. Sagawa, Symmetry energy from the nuclear collective motion: constraints from dipole, quadrupole, monopole and spin-dipole resonances, *The European Physical Journal A* **50**, 10.1140/epja/i2014-14026-9 (2014).
- [30] Z. Zhang and L.-W. Chen, Electric dipole polarizability in ^{208}Pb as a probe of the symmetry energy and neutron matter around $\rho_0/3$, *Phys. Rev. C* **92**, 031301 (2015).
- [31] H. Zheng, S. Burrello, M. Colonna, and V. Baran, Dipole response in neutron-rich nuclei with new skyrme interactions, *Phys. Rev. C* **94**, 014313 (2016).
- [32] J. Xu and W.-T. Qin, Nucleus giant resonances from an improved isospin-dependent boltzmann-uehling-uhlenbeck transport approach, *Phys. Rev. C* **102**, 024306 (2020).
- [33] P.-G. Reinhard, X. Roca-Maza, and W. Nazarewicz, Information content of the parity-violating asymmetry in ^{208}Pb , *Phys. Rev. Lett.* **127**, 232501 (2021).
- [34] A. Klimkiewicz, N. Paar, P. Adrich, M. Fallot, K. Boretzky, T. Aumann, D. Cortina-Gil, U. D. Pramanik, T. W. Elze, H. Emling, H. Geissel, M. Hellström, K. L. Jones, J. V. Kratz, R. Kulesa, C. Nociforo, R. Palit, H. Simon, G. Surówka, K. Sümmerer, D. Vretenar, and W. Waluś (LAND Collaboration), Nuclear symmetry energy and neutron skins derived from pygmy dipole resonances, *Phys. Rev. C* **76**, 051603 (2007).
- [35] A. Carbone, G. Colò, A. Bracco, L.-G. Cao, P. F. Bortignon, F. Camera, and O. Wieland, Constraints on the symmetry energy and neutron skins from pygmy resonances in ^{68}Ni and ^{132}Sn , *Phys. Rev. C* **81**, 041301 (2010).
- [36] V. Baran, B. Frecus, M. Colonna, and M. Di Toro, Pygmy dipole resonance: Collective features and symmetry energy effects, *Phys. Rev. C* **85**, 051601 (2012).
- [37] D. Vretenar, Y. F. Niu, N. Paar, and J. Meng, Low-energy isovector and isoscalar dipole response in neutron-rich nuclei, *Phys. Rev. C* **85**, 044317 (2012).
- [38] X. Roca-Maza, M. Brenna, B. K. Agrawal, P. F. Bortignon, G. Colò, L.-G. Cao, N. Paar, and D. Vretenar, Giant quadrupole resonances in ^{208}pb , the nuclear symmetry energy, and the neutron skin thickness, *Phys. Rev. C* **87**, 034301 (2013).
- [39] P.-G. Reinhard and W. Nazarewicz, Information content of a new observable: The case of the nuclear neutron skin, *Phys. Rev. C* **81**, 051303 (2010).
- [40] J. Piekarewicz, Symmetry energy constraints from giant resonances: A relativistic mean-field theory overview, *The European Physical Journal A* **50**, 10.1140/epja/i2014-14025-x (2014).
- [41] X. Roca-Maza, X. Vinas, M. Centelles, B. Agrawal, G. Colo, N. Paar, J. Piekarewicz, and D. Vretenar, Neutron skin thickness from the measured electric dipole polarizability in ni 68, sn 120, and pb 208, *Physical Review C* **92**, 064304 (2015).
- [42] L.-W. Chen, Private communication (2025).
- [43] W. B. He, Y. G. Ma, X. G. Cao, X. Z. Cai, and G. Q. Zhang, Giant dipole resonance as a fingerprint of α clustering configurations in ^{12}C and ^{16}O , *Phys. Rev. Lett.* **113**, 032506 (2014).
- [44] W. B. He, Y. G. Ma, X. G. Cao, X. Z. Cai, and G. Q. Zhang, Dipole oscillation modes in light α -clustering nuclei, *Phys. Rev. C* **94**, 014301 (2016).
- [45] H.-Y. Kong, J. Xu, L.-W. Chen, B.-A. Li, and Y.-G. Ma, Constraining simultaneously nuclear symmetry energy and neutron-proton effective mass splitting with nucleus giant resonances using a dynamical approach, *Phys. Rev. C* **95**, 034324 (2017).
- [46] R. Wang, Z. Zhang, L.-W. Chen, C. M. Ko, and Y.-G. Ma, Constraining the in-medium nucleon-nucleon cross section from the width of nuclear giant dipole resonance, *Physics Letters B* **807**, 135532 (2020).
- [47] Y.-D. Song, R. Wang, Z. Zhang, and Y.-G. Ma, In-medium nucleon-nucleon cross sections from character-

- istics of nuclear giant resonances and nuclear stopping power, *Phys. Rev. C* **108**, 064603 (2023).
- [48] C. Tao, Y. G. Ma, G. Q. Zhang, X. G. Cao, D. Q. Fang, and H. W. Wang, Pygmy and giant dipole resonances by coulomb excitation using a quantum molecular dynamics model, *Physical Review C* **87**, 10.1103/physrevc.87.014621 (2013).
- [49] J. Xu, J. Zhou, Z. Zhang, W.-J. Xie, and B.-A. Li, Constraining isovector nuclear interactions with giant resonances within a bayesian approach, *Physics Letters B* **810**, 135820 (2020).
- [50] Y.-X. Zhang, Y.-J. Wang, M. Colonna, P. Danielewicz, A. Ono, M. B. Tsang, H. Wolter, J. Xu, L.-W. Chen, D. Cozma, Z.-Q. Feng, S. Das Gupta, N. Ikeno, C.-M. Ko, B.-A. Li, Q.-F. Li, Z.-X. Li, S. Mallik, Y. Nara, T. Ogawa, A. Ohnishi, D. Oliinychenko, M. Papa, H. Petersen, J. Su, T. Song, J. Weil, N. Wang, F.-S. Zhang, and Z. Zhang, Comparison of heavy-ion transport simulations: Collision integral in a box, *Phys. Rev. C* **97**, 034625 (2018).
- [51] A. Ono, H. Horiuchi, T. Maruyama, and A. Ohnishi, Antisymmetrized version of molecular dynamics with two-nucleon collisions and its application to heavy ion reactions, *Progress of Theoretical Physics* **87**, 1185 (1992), <https://academic.oup.com/ptp/article-pdf/87/5/1185/5272175/87-5-1185.pdf>.
- [52] A. Ono, H. Horiuchi, T. Maruyama, and A. Ohnishi, Fragment formation studied with antisymmetrized version of molecular dynamics with two-nucleon collisions, *Phys. Rev. Lett.* **68**, 2898 (1992).
- [53] N. Ikeno and A. Ono, Collision integral with momentum-dependent potentials and its impact on pion production in heavy-ion collisions, *Phys. Rev. C* **108**, 044601 (2023).
- [54] N. Ikeno, A. Ono, Y. Nara, and A. Ohnishi, Probing neutron-proton dynamics by pions, *Phys. Rev. C* **93**, 044612 (2016).
- [55] Y. Kanada-En'yo and M. Kimura, Dipole resonances in light neutron-rich nuclei studied with time-dependent calculations of antisymmetrized molecular dynamics, *Phys. Rev. C* **72**, 064301 (2005).
- [56] Z. Zhang and L.-W. Chen, Isospin splitting of the nucleon effective mass from giant resonances in ^{208}Pb , *Phys. Rev. C* **93**, 034335 (2016).
- [57] D. Adhikari, H. Albatineh, D. Androic, K. Aniol, D. S. Armstrong, T. Averett, C. Ayerbe Gayoso, S. Barcus, V. Bellini, R. S. Beminiwattha, J. F. Benesch, H. Bhatt, D. Bhatta Pathak, D. Bhetuwal, B. Blaikie, Q. Campagna, A. Camsonne, G. D. Cates, Y. Chen, C. Clarke, J. C. Cornejo, S. Covrig Dusa, P. Datta, A. Deshpande, D. Dutta, C. Feldman, E. Fuchey, C. Gal, D. Gaskell, T. Gautam, M. Gericke, C. Ghosh, I. Halilovic, J.-O. Hansen, F. Hauenstein, W. Henry, C. J. Horowitz, C. Jantzi, S. Jian, S. Johnston, D. C. Jones, B. Karki, S. Katugampola, C. Keppel, P. M. King, D. E. King, M. Knauss, K. S. Kumar, T. Kutz, N. Lashley-Colthirst, G. Leverick, H. Liu, N. Liyange, S. Malace, R. Mammei, J. Mammei, M. McCaughan, D. McNulty, D. Meekins, C. Metts, R. Michaels, M. M. Mondal, J. Napolitano, A. Narayan, D. Nikolaev, M. N. H. Rashad, V. Owen, C. Palatchi, J. Pan, B. Pandey, S. Park, K. D. Paschke, M. Petrusky, M. L. Pitt, S. Premathilake, A. J. R. Puckett, B. Quinn, R. Radloff, S. Rahman, A. Rathnayake, B. T. Reed, P. E. Reimer, R. Richards, S. Riordan, Y. Roblin, S. Seeds, A. Shahinyan, P. Souder, L. Tang, M. Thiel, Y. Tian, G. M. Urciuoli, E. W. Wertz, B. Wojtsekhowski, B. Yale, T. Ye, A. Yoon, A. Zec, W. Zhang, J. Zhang, and X. Zheng (PREX Collaboration), Accurate determination of the neutron skin thickness of ^{208}Pb through parity-violation in electron scattering, *Phys. Rev. Lett.* **126**, 172502 (2021).
- [58] E. Chabanat, P. Bonche, P. Haensel, J. Meyer, and R. Schaeffer, A skyrme parametrization from subnuclear to neutron star densities, *Nuclear Physics A* **627**, 710 (1997).
- [59] A. Tamii, I. Poltoratska, P. von Neumann-Cosel, Y. Fujita, T. Adachi, C. A. Bertulani, J. Carter, M. Dozono, H. Fujita, K. Fujita, K. Hatanaka, D. Ishikawa, M. Itoh, T. Kawabata, Y. Kalmykov, A. M. Krumbholz, E. Litvinova, H. Matsubara, K. Nakanishi, R. Neveling, H. Okamura, H. J. Ong, B. Özel-Tashenov, V. Y. Ponomarev, A. Richter, B. Rubio, H. Sakaguchi, Y. Sakemi, Y. Sasamoto, Y. Shimbara, Y. Shimizu, F. D. Smit, T. Suzuki, Y. Tameshige, J. Wambach, R. Yamada, M. Yosoi, and J. Zenihiro, Complete electric dipole response and the neutron skin in ^{208}Pb , *Phys. Rev. Lett.* **107**, 062502 (2011).
- [60] M. Qiu, L.-W. Chen, Z. Z. Li, Y. F. Niu, and Z. Zhang, Symmetry energy and neutron matter equation of state at $\rho_0/3$ from the electric dipole polarizability in ^{48}Ca , ^{68}Ni , and ^{208}Pb , *Phys. Rev. C* **112**, 044312 (2025).
- [61] N. Wang, L. Ou, and M. Liu, Nuclear symmetry energy from the fermi-energy difference in nuclei, *Phys. Rev. C* **87**, 034327 (2013).
- [62] W. Lynch and M. Tsang, Decoding the density dependence of the nuclear symmetry energy, *Physics Letters B* **830**, 137098 (2022).
- [63] P. Morfouace, C. Tsang, Y. Zhang, W. Lynch, M. Tsang, D. Coupland, M. Youngs, Z. Chajacki, M. Famiano, T. Ghosh, G. Jhang, J. Lee, H. Liu, A. Sanetullaev, R. Showalter, and J. Winkelbauer, Constraining the symmetry energy with heavy-ion collisions and bayesian analyses, *Physics Letters B* **799**, 135045 (2019).
- [64] C. Drischler, K. Hebeler, and A. Schwenk, Asymmetric nuclear matter based on chiral two- and three-nucleon interactions, *Phys. Rev. C* **93**, 054314 (2016).
- [65] C. Ciampi, S. Mallik, F. Gulminelli, D. Gruyer, J. Frankland, N. Le Neindre, R. Bougault, A. Chbihi, L. Baldesi, S. Barlini, B. Borderie, A. Camaiani, G. Casini, I. Dekhissi, J. Dueñas, Q. Fable, F. Gramegna, M. Henri, B. Hong, S. Kim, A. Kordyasz, T. Kozik, I. Lombardo, O. Lopez, T. Marchi, S. Nam, J. Park, M. Pârlog, G. Pasquali, S. Piantelli, G. Poggi, S. Valdré, G. Verde, and E. Vient, Constraining the nuclear symmetry energy with fermi-energy heavy ion collisions, *Physics Letters B* **868**, 139815 (2025).
- [66] L.-W. Chen, B.-J. Cai, C. M. Ko, B.-A. Li, C. Shen, and J. Xu, Higher-order effects on the incompressibility of isospin asymmetric nuclear matter, *Phys. Rev. C* **80**, 014322 (2009).
- [67] C. Xu, B.-A. Li, and L.-W. Chen, Symmetry energy, its density slope, and neutron-proton effective mass splitting at normal density extracted from global nucleon optical potentials, *Phys. Rev. C* **82**, 054607 (2010).